Modeling O(^{3}P) and Ar Scattering from the Ionic Liquid [emim][NO_3] at 5 eV with Hybrid QM/MM Molecular Dynamics†

Scott Yockel and George C. Schatz*

Department of Chemistry, Northwestern University, 2145 Sheridan Road, Evanston, Illinois 60208-3113

Received: November 10, 2009; Revised Manuscript Received: February 5, 2010

In this paper, we develop a hybrid QM/MM-MD direct dynamics method for the study of Ar and O scattering from room-temperature ionic liquids (RTIL) at hyperthermal energies, with the goal of providing an understanding of the reactivity of ionic liquids as potential hypergolic fuels. The RTIL is chosen to be 1-ethyl-3-methylimidazolium nitrate ([emim][NO_3]) as the bulk properties of this have been analyzed experimentally and theoretically, and a force field has been developed. Within our simulation time of 7.3 ps, Ar collisions with the liquid surface cause 2−3 proton transfers to occur from the imidazolium ring to the anion, and a small fraction of these events leads to the desorption of neutral "emim" or HNO_3 species. These charge-transfer processes also occur for O(^{3}P) collisions, but in addition, there is a rich amount of chemical change at the surface leading to four main collision types, reaction with NO_3 to form species like [NO_2] and O_2, O addition to the imidazolium ring causing ring scission, H abstractions from the hydrocarbon chains (ethyl or methyl) or imidazolium ring generating OH, and O atom inelastic scattering. Within the MSINDO model, the major scattered products (all are neutral) from the O collisions, with their probabilities in parentheses, are O (0.13), emim (0.12), HNO_2 (0.05), HNO_3 (0.04), and OH (0.04). Of these products, only OH is unique to O atom collisions; the HNO_2 and HNO_3 products also arise when the incident atom is Ar or O.

I. Introduction

Room-temperature ionic liquids (RTIL) are materials composed of cations and anions that are liquids below an arbitrarily defined temperature (usually 100 °C). Although RTIL have been known since 1914,[1] their application was limited until the 1990s because the use of moisture-sensitive anions forced preparation and experiments to be performed inside of a glovebox. Today, RTIL can be formed by a number of stable cation/anion pair combinations, including imidazolium $[im]^+$, pyridinium $[P]^+$, pyrrolidinium $[Pyr]^+$, and the anions are usually atomic halides, small noncoordinating anions (e.g., $[BF_4]^-$, $[PF_6]^-$) or other larger less toxic organic anions (e.g., bistriflimide $[NTf_2]^-$, triflate $[OTf]^-$, tosylate $[OTs]^-$). One of the most frequently studied cations is 1,3-dialkylimidazolium, including 1-ethyl-3-methylimidazolium or [emim]. Generally, these liquids are nonvolatile and nonflammable, chemically and thermally stable, and possess high ionic conductivity. Due in part to these properties and to the relative customization of these liquids, there has been a huge increase in their study and use.[2] Applications of RTIL include replacement of volatile organic solvents and dipolar aprotic solvents,[3,4] storage media for gases (CO_2, SO_2, BF_3, PH_3)[5,6] and hydrogen fuel cells,[7] solvent for nuclear fuel processing[8] and cellulose processing,[9] and heat transfer media in solar thermal energy systems.[10] In addition, RTIL have been considered as possible propellants in cone-jets and as environmentally conscious hypergolic bipropellants.[11−13] In many of these new applications, reactions at the surface/interface of the RTIL play an important role; however, there have been few studies of these reactions, and the mechanisms are not understood.

Characterization of the reactivity of the RTIL surfaces involves understanding many properties of the surface (e.g., surface topology, electronic states of various ionic species, charge distribution including the response to charge transfer, influence of the bulk properties, effects of impurities, and so forth). Direct recoil spectroscopy (DRS) and sum-frequency generation (SFG) studies have provided much insight to the surface orientation of the cations and anions. Seddon et al.[14] and Watson et al.[15,16] provided some of the first studies on RTIL surfaces using DRS to study [bmim][PF_6] and later [bmim][BF_4]. They found both the cation and anion present at the surface, with the imidazolium ring oriented perpendicular to the surface and the butyl chain parallel to the surface in [bmim][PF_6] and stuck down into the bulk in [bmim][BF_4]. Numerous SFG experiments suggest that the imidazolium ring lays parallel to the surface, with the alkyl chain protruding away from the surface.[17,18] While studying short-chain [emim] and [mmim] cations with larger anions (methyl sulfate), Santos and Baldelli concluded that there must be some balance in the Coulombic interaction and the dispersion forces that effect the local orientation of the cation and anion at the surface.[19] Recent advances in SFG have allowed Iwahashi et al. to show the existence of a polar ordering at the surface of [bmim][OTf], in which the nonpolar CF_3 groups of the anion stick out of the surface, giving a distinct order to the attached SO_3 group.[20] They further suggested that the SO_3 groups are likely hydrogen-bonded to the [bmim] cation. In addition, the surface orientation can be influenced by the local environment. Baldelli et al. have shown that wetting the surface of [bmim]-containing RTIL caused the ring portion to reorient and stand on end.[21]

Theoretical modeling has also proven to be instrumental in understanding the physiochemical properties of RTIL. For molecular dynamics (MD) simulations, empirical potential models of the various cation and anion pairs have only recently been developed. The sophistication of these models ranges from coarse-grained molecular sites to polarizable all-atom force fields. In a study that compares a standard all-atom force field

† Part of the "Michael R. Wasielewski Festschrift".

* To whom correspondence should be addressed. E-mail: schatz@chem.northwestern.edu.

10.1021/jp910707v
Published on Web 03/08/2010

to their newly developed polarizable force field, Voth et al. showed that the latter has little effect on the surface topology of the ionic liquid surface, while the effects on surface tension are more substantial.[22] In comparison to the SFG studies discussed above on [bmim]-containing RTIL surfaces, the theoretical models are in agreement in that they find the alkyl chains to protrude from the surface.[23,24] Additionally, each of these studies predicts that the imidazolium ring orients at the surface with an angle between 35 and 65°, which matches most of the experimental data except those involving the $[BF_4]$ anion. Although some modeling has characterized the physical properties of the surfaces of a number of RTIL, few if any studies have been completed on the chemical reactivity at RTIL surfaces.

In the past, the scattering of gaseous atoms off of liquid surfaces has provided a useful tool for understanding surface reactivity.[25−35] Computing the chemical dynamics of collisions in the gas phase using direct dynamics has recently been extended to modeling the gas−liquid interface using a type of hybrid quantum mechanics/molecular mechanics (QM/MM) "on-the-fly" simulation method.[36] Previously, our group has applied this method to study $O(^3P)$ and $F(^2P)$ atom scattering from squalane ($C_{30}H_{62}$) surfaces at hyperthermal (5 eV) energies.[37,38] In the current study, we use this method to assess collisions of Ar and $O(^3P)$ with a RTIL surface that we choose to be $[emim][NO_3]$. $[emim][NO_3]$ was chosen because it represents a possible hypergolic bipropellant, and it also limits the number of different types of atomic interactions to C, H, N, and O. In addition, an all-atom force field exists for this liquid. The choice of Ar and $O(^3P)$ enables us to compare a purely nonreactive rare gas atom with a strongly reactive atom, thereby determining the dominant reactions that are chemically induced with reactions that are physically induced. Similar experimental collision studies on $O(^3P)$ + $[emim][NTf_2]$ and $[C_{12}mim][NTf_2]$ have been performed by Minton et al. with an analysis of the desorption products and modeling of the surface structure.[39] The present work, which was done in tandem, provides the first study describing the chemical reactions at the gas−liquid interface of RTIL.

II. Methodology

Prior to simulation of the scattering experiment, a model $[emim][NO_3]$ surface must be created, as we now describe. For all MM computations, the all-atom OPLS-AA type force field from Canongia Lopes et al. was utilized.[40,41] The initial structure for the bulk simulation was taken from the Cambridge Crystallographic Database (CCDB) reference KUCPED,[42] which contains four ion pairs and was replicated to form a $6 \times 2 \times 2$ stack of cells for a total of 96 ion pairs (2208 atoms). During the bulk and surface-only simulations, the following parameters were chosen using the TINKER[43] code: periodic boundary conditions (PBC), 1.0 fs time step, cutoffs of nonbonded forces at 10.0 Å, Nosé−Hoover thermostat, and Ewald summation. In order to equilibrate the bulk temperature from the initial crystal structure, a *NVT* ensemble was run for 100 ps at 500K and then for 500 ps for a *NPT* ensemble at 1.0 atm to ensure that the density had equilibrated. Next, the temperature was lowered to 298 K, and 1.0 ns of the *NPT* ensemble gave an average density of 1.31 g/cm^3, which overestimates the experimental crystalline density by ∼2.4%. In order to simulate the surface, the PBC box size was extended 3-fold in the *a*-axis direction to create empty space above and below the existing bulk structure; this effectively removed the periodic boundary in one direction. The surface simulations were run starting with this structure at 298 K for 1.0 ns with a *NVT* ensemble, after which the average surface density and molecular orientation for the last 500 ps were computed. For clarification, during the subsequent collision studies, the MM portion of the computation does not contain a PBC or Ewald summation. It is thought that not utilizing the Ewald summation during the QM/MM-MD simulations has little effect on the outcome of the hyperthermal collision events since only small energetic long-range interactions are absent for the MM portion and the main collision interaction is described by the QM portion of the surface.

In order to gain insight into the chemical reactivity of the surface upon collision with a gaseous species, the dynamical processes of bond-making and -breaking events must be well-described. However, computing these processes from first-principles QM becomes very computationally expensive for more than ∼20 non-hydrogen atoms, especially when thousands of trajectories must be done for good statistics. Therefore, we have chosen to use the QM/MM-MD approach previously developed by our group which utilizes the QM method MSINDO, the modified symmetrically orthogonalized intermediate neglect of differential overlap form of a semiempirical Hamiltonian.[44,45] In our prior computations involving the squalane surface, MSINDO has provided reliable results for the translational and vibrational energy of the desorption products, with a slight overestimation of their rotational energy.[37,38] In this study, we continue to use MSINDO as our QM method as earlier studies have shown that it outperforms other standard semiempirical methods when computing the electronic properties of nitrogen-containing ring systems similar to our [emim].[46,47] For an understanding of the energetics in our $O(^3P)$ + $[emim][NO_3]$ study, we have computed reaction energies for the most common reactions; the results are provided in the Supporting Information Table S1.

Unlike our previous QM/MM studies of gas/liquid scattering, in this study we have eliminated the use of the dynamic partitioning of atoms between the QM and MM regions. Having ions cross between different regions (QM and MM) is not well-suited for our current application as it would require dividing the imidazolium ring and/or nitrate into QM and MM parts and redetermining MM charges on the fly. After testing numerous trajectory paths, we decided to fix the QM region to include five ion pairs (115 atoms) at or near the surface and the incident $O(^3P)$ atom. Because the surface density of $[emim][NO_3]$ is very high (nearly double that of squalane), it is rare that the incident atom with an $E_T \leq 5.0$ eV has a direct interaction with more than the first two ion pair layers. Thus, unlike squalane, where there often were several well-separated radical species, $O(^3P)$ + $[emim][NO_3]$ can be treated with a more localized QM description.

For each collision trajectory, the surface consisted of a box that was $32.3 \times 34.5 \times 31.6$ Å^3. Because a PBC was not used, the atomic coordinates that reside in a 5.0 Å thick region on the sides and bottom of the box were kept fixed during the simulation, as depicted in the Supporting Information Figure S1. This fixed region prevents the box from losing its shape, which would drastically change the density of the liquid, thus affecting interactions with the incident atom. Ten random snapshots of the equilibrated surface were used as the initial surface structures for the trajectory simulations. For the collision simulation, the PBC box coordinates perpendicular to the surface (referred to as the *a*-axis) were shifted so that the $x = 0$ plane represented the area where the surface density is equal to half of the bulk value (the Gibbs dividing surface). Furthermore, the $x = 0$ plane was considered as the defining plane where the

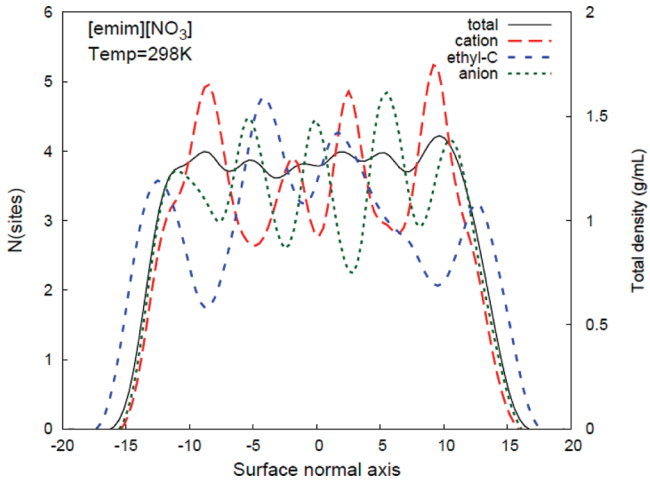

Figure 1. The average total density, in g/mL, (right axis) and the component number density (left axis) of [emim][NO_3] at 298 K. The surface-normal axis (in Å) is the *a*-axis in the PBC box, not to be confused with the *x*-axis in the collision simulations, which have had their coordinates shifted.

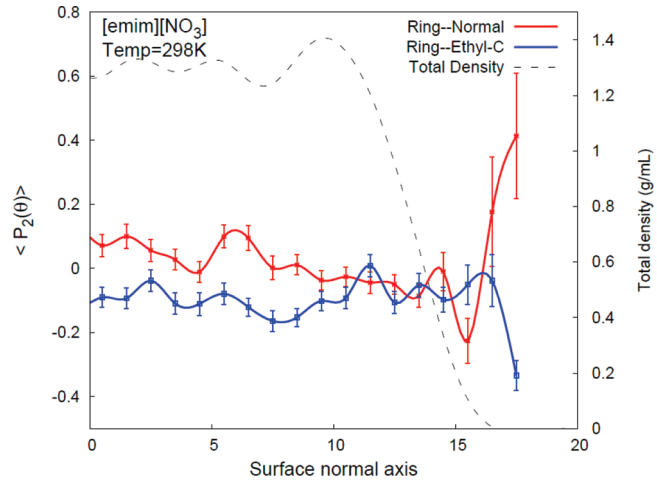

Figure 2. Average second Legendre polynomial $\langle P_2(\theta)\rangle = 1/2\ (3\cos^2\theta - 1)$, where θ is the angle between the surface-normal and the specified vector. The total density, in g/mL (dashed line) is overlaid in this graph for comparison. The surface-normal axis (in Å) is the *a*-axis in the PBC box, not to be confused with the *x*-axis in the collision simulations, which have had their coordinates shifted.

incident atom enters or leaves the surface and was used for determining the time spent in the liquid phase. The incident atom O(^{3}P) was included in the QM region and started 8.0 Å above the surface with an initial translational energy of 5.0 eV. On the other hand, the Ar incident atom with an initial E_T of 5.0 eV was always kept in the MM region and essentially acted as a nonreactive perturbation to the [emim][NO_3] surface kinetic energy. This allowed us to examine the difference in reactivity of the liquid with itself and with a highly reactive atomic source. Each of the incident atoms collided with each surface in a square grid of nine points, each separated by 2.5 Å and centered at the surface origin. The spacing of 2.5 Å was chosen because it is the average "width profile" of each of the molecular species (NO_3, imidazolium ring, and ethyl chain) and is thought to allow sampling of different chemically relevant areas on a single surface. At each of these nine sites, the incident atoms struck the surface with four different angles relative to the surface-normal (θ = 0, 30, 45, and 60°) and with four different azimuthal angles (φ = 0, 90, 180, and 270°) as we have done previously.[37,38] This allows for 117 trajectories on each surface structure and totals 1170 collisions for each incident atom, O(^{3}P) and Ar. Each reaction was terminated if either a QM product reached more than 20 Å above the surface or if the total simulation time exceeded 7.3 ps. In all statistical values provided in the tables and figures, the error bars for each value listed were calculated as the standard error of the mean, which is equal to the sample standard deviation divided by the square root of the sample size.

III. Results and Discussion

A. Ionic Liquid Surface. In order to characterize the surface topology of our [emim][NO_3] model surface, we used the last 500 ps of the NVT surface-only simulations to generate an average surface density distribution (Figure 1) and molecular orientation (Figure 2). In Figure 1, the total density is shown as a function of distance (in 1.0 Å slices) along the surface-normal (*x*-axis). This shows a slight increase in the total density at the surface, which is comparable to what has been seen in other surface models of RTIL.[24,48−50] In addition, three molecular sites are designated in Figure 1 in which "cation" corresponds to the center-of-mass of the imidazolium ring (not including the methyl and ethyl), the "ethyl-C" is the CH_3 carbon of the ethyl group, and "anion" is the N of [NO_3]. As Voth et al. have shown for [emim][NO_3],[50] we have also found the anion slightly more abundant at the surface than the cation, which is also similar to [bmim][PF_6].[48] The ethyl carbon distinctly sticks out of the surface, being the only molecular species that extends beyond the Gibbs dividing surface. This is a logical result as ethyl is the largest nonpolar group, and it can easily orient away from the polar environment within the liquid. The average molecular orientation is shown in Figure 2 for the imidazolium ring normal vector (ring−normal) and for a vector from the ring N containing the ethyl group to the CH_3 of the ethyl group (ring−ethyl-C). The *y*-axis in the plot ($\langle P_2(\theta)\rangle$) is defined as the average second Legendre polynomial $1/2\ (3\cos^2\theta - 1)$, where θ is the angle between the surface-normal and the vector of the molecular species specified within Figure 2. Beneath the surface, there is no preferred orientation; however, beyond 15 Å from the center of the slab, the ethyl groups stick out of the surface, and the rings have a preferential orientation with a slight tilt. This agrees with earlier studies; therefore, our model surface still captures the topological features of other larger models.

B. Ar Collision Results. To understand the chemical reactivity of the [emim]][NO_3] surface with minimal chemical influence of the colliding atom, we first investigate the effects of an incident hyperthermal Ar. We find that, in general, upon collision, there is a small amount of chemical change in the surface, which supports the idea that ionic liquids are relatively stable. In Table 1, the average probability of any non-Ar desorption products (row labeled "average") within the limits of our simulation time is 0.17, of which there is only a slight variation in desorbed product with respect to the Ar incident angle. There is a high probability, 0.91, that the Ar desorbs from the surface within 7.3 ps, and this probability is independent of incident angle. There is the possibility that this value is underestimated due to the fact that a small fraction of desorbed products leaves the surface at an angle larger than 90° from the surface-normal and therefore remains below our desorption cutoff (x = 3.0 Å).

Of the non-Ar products that desorb from the surface, each is the result of a proton transfer from a hydrogen on the imidazolium ring to the anion. The deprotonated cation, (referred to without the brackets as emim) leaves the surface almost twice as often as HNO_3. Additionally, there is a small fraction (0.01)

TABLE 1: Scattering Probabilities for Nonreactive Ar + [emim][NO_3] and Distribution of Each Nascent Product by the Angle of Incidence

	average	$\theta_i = 0°$	30°	45°	60°
total[a]	0.17 ± 0.01	0.18 ± 0.04	0.17 ± 0.02	0.16 ± 0.02	0.19 ± 0.02
incident Ar	0.91 ± 0.03				
HNO_3	0.06 ± 0.01	0.08 ± 0.03	0.08 ± 0.01	0.04 ± 0.01	0.06 ± 0.01
emim[b]	0.10 ± 0.01	0.10 ± 0.03	0.08 ± 0.02	0.11 ± 0.02	0.12 ± 0.02
emim + [NO_3][c]	0.01 ± 0.003	0.00	0.01 ± 0.01	0.01 ± 0.01	0.01 ± 0.01

[a] Includes the sum of all non-Ar products. [b] Refers to the neutral species from the cation [emim] after loss of H^+. [c] Refers to any pairs or groups of the imidazolium ring (cation or neutral) with the anion.

TABLE 2: Distribution of the Number of Proton Transfers and Cation/Anion Pair Recombinations

proton transfer	incident O	incident Ar
0	0.12 ± 0.01	0.13 ± 0.01
1	0.29 ± 0.02	0.21 ± 0.01
2	0.35 ± 0.02	0.31 ± 0.02
3	0.20 ± 0.01	0.30 ± 0.02
4	0.04 ± 0.01	0.05 ± 0.01
5	0.00	0.00
[emim] + [NO_3] → emim−ONO_2[a]	0.12 ± 0.01	0.12 ± 0.01

[a] An oxygen from NO_3 attaches to the imidazolium ring.

TABLE 3: Mean Depths of Penetration of the [emim][NO_3] Surface (in Å) from Incident Ar and O(^{3}P) with a Translational Energy (E_T) of 5.0 eV from Incident Angles 0, 30, 45, and 60°

	$\theta_i = 0°$	30°	45°	60°
Ar	−0.66 ± 0.18	−0.06 ± 0.09	0.40 ± 0.09	0.94 ± 0.09
O	−2.85 ± 0.17	−2.26 ± 0.09	−1.54 ± 0.09	−0.68 ± 0.08

of the collisions that leads to desorption of more than one molecular species or a small cluster of molecules. These are denoted *emim* + [NO_3] where "*emim*" could be either the charged cation [emim] or neutral emim. This is not to be confused with the desorption of a single ion species, which was never observed. The distribution of the number of proton transfers for each trajectory (independent of what other processes occur) is shown in Table 2. The theoretical maximum for proton transfer in our simulation is five because only five cation/anion pairs exist in the QM region. For the incident Ar, the majority of trajectories have an average of 2−3 proton transfers. In addition to proton transfer, our model shows a small (0.12) probability for cation/anion pairs to combine into a neutral species. This normally occurs when an oxygen on the anion binds to a carbon on the imidazolium ring and is therefore referred to as emim−ONO_2.

The mean residence time and depth of penetration allow for a further understanding of the gas−surface dynamics, including the rigidity of the surface. As shown in Table 3, only when the incident angle is at 0° is the average penetration depth of Ar below $x = 0$. This demonstrates that even when the incident atom contains 5.0 eV of kinetic energy, which is more than is needed to break bonds, the ionic liquid surface remains relatively rigid and chemically stable. In Table 4, the mean residence times are defined as the time the incident atom spends beneath the $x = 0$ surface. For Ar, Table 3 shows that the residence times are smaller at larger incident angles, just as the penetration depths are shallower. We also computed the probability that the incident atom does not cross $x = 0$, denoted $P(\tau{=}0)$. For incident Ar, most of the trajectories result in Ar never crossing the surface and thus interacting only with the top of the surface. When Ar does break through the $x = 0$ plane, it has a longer residence time than the previous simulation models of O(^{3}P) or

TABLE 4: Mean Residence Times ($\langle\tau_{res}\rangle$, in fs) from Incident Ar and O(^{3}P) with a Translational Energy (E_T) of 5.0 eV from Incident Angles 0, 30, 45, and 60° [a]

	$\theta_i = 0°$	30°	45°	60°
Ar	1487 ± 269	1260 ± 131	1134 ± 157	1083 ± 239
$P(\tau{=}0)$	0.4	0.5	0.6	0.8
O	4807 ± 254	4721 ± 135	4065 ± 145	3606 ± 163
$P(\tau{=}0)$	0.0	0.0	0.1	0.2

[a] $P(\tau{=}0)$ represents the probability that the incident atom does not cross the surface ($x = 0$).

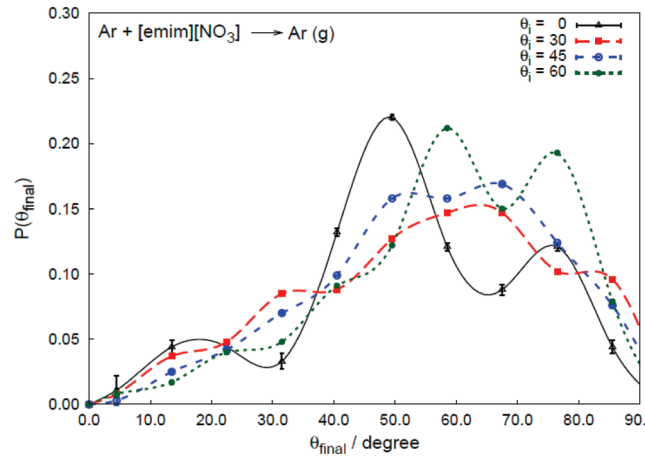

Figure 3. Distribution of the final scattering angle of Ar with respect to surface-normal for incident angles (θ_i = 0, 30, 45, and 60°).

F(^{2}P) scattering with a squalane surface, with nearly double the time of the inelastic collision or H-abstraction products.[37,38]

To connect with related molecular beam studies that have been performed by Minton and co-workers[39] on [emim][NTf_2], we have also computed the distribution of final scattering angles (Figure 3) and translational energies (Figure 4). For each angle of incidence, there is a relatively broad distribution of the final scattering angles, which is indicative of a rough surface, similar to what has been seen in our previous studies with the squalane surface.[37,38] Regardless of the incident angle, there is a general trend that the Ar scatters to a final angle that is predominantly between 50 and 80° from the surface-normal. This likely reflects the influence of the oriented imidazolium rings at the surface on the final scattering angle of the nonreactive incident atom. For the translational energy distribution of Ar, more direct impacts commonly result in greater loss of translational energy. This trend, which is closely related to the residence times and penetration depth, is understandable since for $\theta_i = 0°$, the Ar atom has more time for and a greater number of direct atomic interactions, causing further relaxation in its final translational energy. Even at incident angles of 60°, roughly half of the incident energy is lost, which is similar to what has been found experimentally with the inelastically scattered O + [emim][NTf_2].[39]

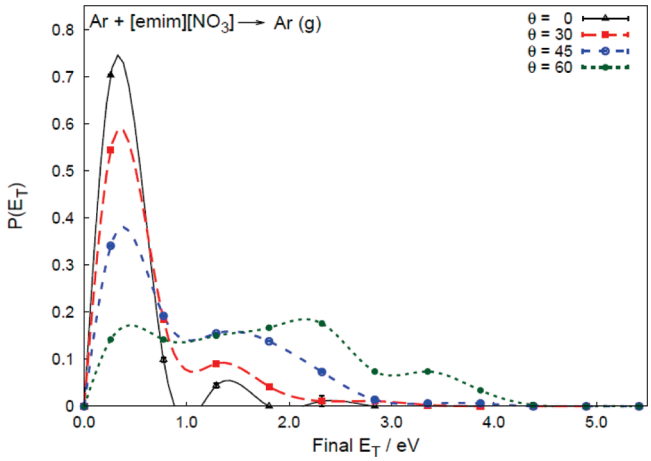

Figure 4. Distribution of the final translational energy (in eV) of Ar for each incident angle (θ = 0, 30, 45, and 60°).

TABLE 5: Reaction Probability from O(^{3}P) + [emim][NO_3] by Reaction Type

distribution of reactions by type	
O scattering	0.13 ± 0.01
O addition to NO_3	0.02 ± 0.004
elimination of NO_3	0.43 ± 0.02
O addition to HC[a]	0.01 ± 0.002
elimination of HC from ring	0.04 ± 0.01
ring scission−O addition[b]	0.21 ± 0.01
ring fragmentation−O addition[c]	0.05 ± 0.01
H abstraction	0.09 ± 0.01
NO_3 substitution	0.01 ± 0.003
HC substitution−H elimination	0.02 ± 0.004

[a] HC refers to the ethyl or methyl hydrocarbon on the imidazolium ring. [b] After ring scission, the [emim] becomes an intact chain. [c] After becoming a chain, fragmentation occurs.

C. O(^{3}P) Collision Results. In contrast to the collisions of Ar with [emim][NO_3], the O(^{3}P) atom causes rich chemical interactions with the surface. In general, the O atom can make a new bond (insertion), break an existing bond (scission), cause secondary reactions in addition to making or breaking bonds, or not react at all and scatter back into the gas phase. Each of these events can involve the O atom interacting with NO_3, the imidazolium ring, or the hydrocarbon (ethyl or methyl) as a primary or secondary collision event. Table 5 summarizes these different types of reactions and includes the possibility that the event occurs from reaction of the initial O atom or from a subsequent reaction. A brief description of the reaction types is given in Table 5, and a more detailed description is in the Supporting Information Table S2. O atom inelastic scattering off of the surface is the third most probable collision type and occurs much less often than that for Ar. In the addition of O to the NO_3, the incident O binds to one of the oxygens of the anion with a small probability of 0.02. The most prevalent reaction channel is the elimination of NO_3, which normally leads to one of two products, NO_2 or HNO_2 and O_2 or, less frequently, OOH. When the O atom adds to a hydrocarbon group, an alcohol is normally formed. However, this is the one of the most infrequent reaction types. When the incident O collides with the atoms on the imidazolium ring, occasionally, ring scission occurs, whereby the addition of the O atom to the ring is followed by an unfolding of the ring into a chain. Sometimes during the process of ring unfolding into a chain, the ring breaks apart into fragments with a probability of 0.05. The probability of formation of intact chains, denoted as ring scission−O addition, is 0.21. In both of the ring scission reactions, the products mostly result in the formation of some type of aldehyde. Hydrogen abstraction (to give OH) normally occurs from the hydrocarbons but can also happen from the imidazolium ring. There is a small fraction of the collisions with NO_3 that result in a substitution of the incident O with an oxygen from the anion, at which point a secondary collision may occur or the new O atom can desorb. Also, when the incident O collides with the end of the CH_3 group of the hydrocarbon, the incident atom can be added, eliminating a H and creating R−CH_2O. This process is familiar from the O + squalane studies. Overall, almost 90% of the reactions result in one of four channels, elimination of NO_3, ring scission−O addition, inelastic O scattering, or H abstraction.

In addition to the rich chemistry that occurs in O(^{3}P) collisions with the surface, proton transfer also occurs. As shown in Table 2, these proton-transfer processes and cation/anion pair recombinations occur with similar magnitude and distribution for O and Ar collisions. On average, each O collision causes 1−2 proton transfers, which is slightly less than Ar. This likely arises because most O collisions lead to other types of chemical reactions, and thus, the energy from a collision is used to break bonds as well as cause proton transfer. In Table 3, as compared to Ar, on average, the incident O penetrates the surface about 2.0 Å deeper for each incident angle. This probably correlates with the fact that the O atom has a smaller van der Waals radius by ~20%. However the ionic liquid is quite dense, and as a result, the O atom depth of penetration is less for [emim][NO_3] than that for the previously studied squalane surface.[37] A consequence of O atom penetration into the dense ionic liquid is that the average residence times for the incident O are much larger than those for Ar, as shown in Table 4, and for the O + squalane results found previously.[37] Indeed, a substantial amount of reacted incident O remains in the surface at the end of the 7.3 ps simulation.

In comparison to the nonreactive Ar collisions, O(^{3}P) collisions with the [emim][NO_3] surface cause a significant increase not only in the fraction of chemical reactions but also in the amount of desorbed products. As shown in Table 6, over half of all of the trajectories result in some type of product desorbing from the surface. This value includes overcounting from multiple desorption events within a single trajectory and would be 0.49 if counting trajectories as a whole. Furthermore, even if the scattered O atoms were subtracted from this, a probability of 0.44 exists for nascent product desorption to occur, which is more than three times that resulting from Ar collisions. Nearly a quarter of all trajectories that result in a scattered product contain the incident O, that is, almost half of all products that desorb from the surface contain the incident O. Since the probability of scattered O is 0.13, then only 0.10 of the desorbed products containing the incident O are a molecular species, likely O_2 or OH. In comparison to the scattered molecular products from the Ar collision listed in Table 1, similar amounts of HNO_3, emim, and *emim* + [NO_3] desorb from the surface. Each of these desorbed species is a product of a proton transfer and occurs in similar amounts in both the reactive and nonreactive collisions. Other small scattered nascent molecular species from the O atom collision include OH, O_2, and HNO_2, all being neutral species. The production of OH is largely from the H abstraction, which has a reaction probability of 0.09. Thus, nearly half of all OH that is created desorbs from the liquid within our simulation time. Similarly, when the incident O causes elimination of a hydrocarbon from the ring, half of these products desorb from the surface with a probability of 0.02. These scattered products, namely, the Me/Et fragment, consist mainly of CH_3, CH_3CH_2, or CH_3O. The unfolded imidazolium

TABLE 6: Scattering Probabilities for Reactive O(^{3}P) + [emim][NO_3] and the Distribution of Each Desorption Product by Angle of Incidence

	average	$\theta_i = 0°$	30°	45°	60°
total[a]	0.57 ± 0.02	0.48 ± 0.07	0.53 ± 0.04	0.55 ± 0.04	0.64 ± 0.04
incident O[b]	0.23 ± 0.01				
HNO_3	0.04 ± 0.006	0.03 ± 0.02	0.05 ± 0.01	0.03 ± 0.01	0.04 ± 0.01
emim	0.12 ± 0.01	0.14 ± 0.04	0.16 ± 0.02	0.12 ± 0.02	0.08 ± 0.02
emim + [NO_3][c]	0.05 ± 0.006	0.03 ± 0.02	0.05 ± 0.01	0.06 ± 0.01	0.03 ± 0.01
O	0.13 ± 0.01	0.02 ± 0.02	0.06 ± 0.01	0.11 ± 0.02	0.23 ± 0.03
OH	0.04 ± 0.005	0.00	0.03 ± 0.01	0.04 ± 0.01	0.05 ± 0.01
O_2	0.02 ± 0.005	0.04 ± 0.02	0.01 ± 0.01	0.02 ± 0.01	0.04 ± 0.01
HNO_2	0.05 ± 0.007	0.08 ± 0.03	0.05 ± 0.01	0.07 ± 0.01	0.04 ± 0.01
Me/Et fragment[d]	0.02 ± 0.005	0.02 ± 0.02	0.01 ± 0.01	0.03 ± 0.01	0.03 ± 0.01
IM chain[e]	0.01 ± 0.003	0.00	0.01 ± 0.01	0.01 ± 0.01	0.01 ± 0.01
IM chain fragment[f]	0.04 ± 0.006	0.08 ± 0.03	0.06 ± 0.01	0.03 ± 0.01	0.04 ± 0.01

[a] Includes all desorption products. [b] Includes only desorption products containing the incident O atom. [c] Refers to any pairs or groups of the imidazolium ring (cation or neutral) with the anion. [d] Methyl or ethyl fragment from elimination of HC from the ring. [e] The unfolded imidazolium ring from ring scission−O addition. [f] A piece of the unfolded ring from ring fragmentation−O addition.

ring or "IM chain" from the scission due to the O addition is the second most abundant reaction channel. However, very little of the products resulting from this reaction channel desorb from the surface within the maximum simulation time allowed. In addition, most of the IM chain products remain charged and would therefore require a much larger force to overcome Coulombic attraction to the anions throughout the liquid. On the other hand, 80% of the products that occur from the fragmentation of the IM chain desorb from the surface. One limitation of our model that may cause an overestimation of the probability of scattered products is that the width of our surface is truncated at some finite distance. When a product escapes the surface with a small amount of translational energy or at a large angle ($\theta_f > 60°$), there is no surface for it to be attracted to, whether from stronger Coulombic or weaker van der Waals forces.

In contrast to the variation in molecular product distribution with incident angle for the Ar collisions as discussed earlier, there is a less distinguishable trend in the desorbed molecular products from the O collisions. The inelastically scattered O, however, is strongly dependent upon incident angle, nearly doubling in probability in going from 0 to 30, to 45, and to 60°. Another conclusion that can be drawn from the incident angle dependence of the results involves the IM chain and IM chain fragment. It appears that when the incident angle is 0° and provides the most force upon impact, imidazolium ring scission frequently leads to fragmentation and then desorption. However for higher angles of incidence, fragmentation is less important.

The distribution of the final scattering angles has been computed for the scattered O product, and the results are presented in Figure 5. Results for $\theta_i = 0°$ are not shown because the statistical uncertainty is too high to make the results meaningful. Furthermore, the O scattered results from $\theta_i = 30°$ have large error bars as they are from only 22 data points. In comparison with the scattered Ar, the scattered O atom tends to have broader distributions, with the majority of the distribution between 30 and 80°. The angular distribution of scattered O from simulation is similar to the experimental observations for O scattered from a [emim][NTf_2] surface.[39] Notable in Figure 5 is the high probability for producing high scattering angles, especially from $\theta_i = 45$ and 60°. The previous simulations with squalane[37] resulted in inelastic scattering of O with narrower angular distributions that were peaked closer to the surface-normal.

The final translational energy distributions for O and OH are presented in Figures 6 and 7, respectively. In the Supporting

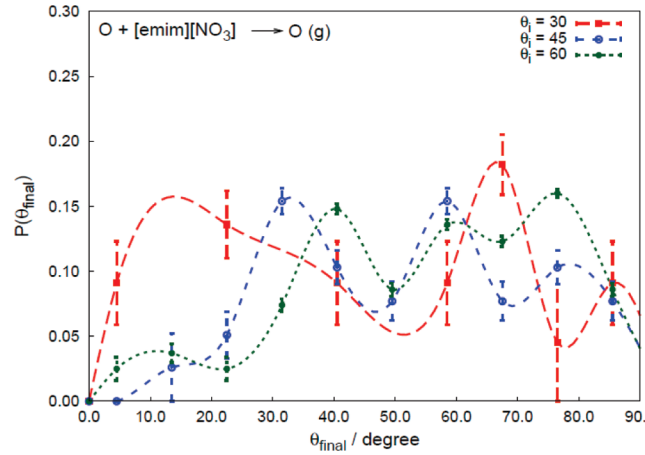

Figure 5. Distribution of the final scattering angle of scattered O with respect to surface-normal for incident angles (θ_i = 30, 45, and 60°).

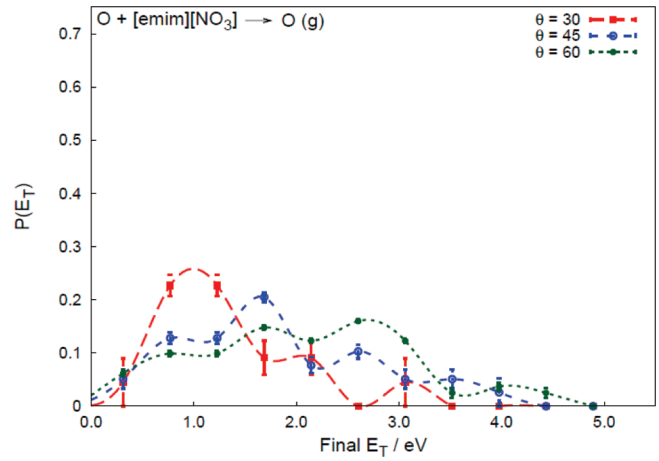

Figure 6. Distribution of the final translational energy (in eV) of O for incident angles (θ = 30, 45, and 60°).

Information, the final translation energy distribution plots for HNO_2 and HNO_3 can be found in Figures S2 and S3, respectively. Each plot includes results for incident angles of 30, 45, and 60°. These figures show that the scattered O has a slightly broader distribution of final translational energies in comparison to the scattered Ar (Figure 4). The OH scattering has a very similar distribution to that of the O scattering, but overall, there is a small loss (~0.5 eV) in final translational energy. The average final translational energy for both O and OH for $\theta_i = 60°$ is roughly half of the initial translational energy

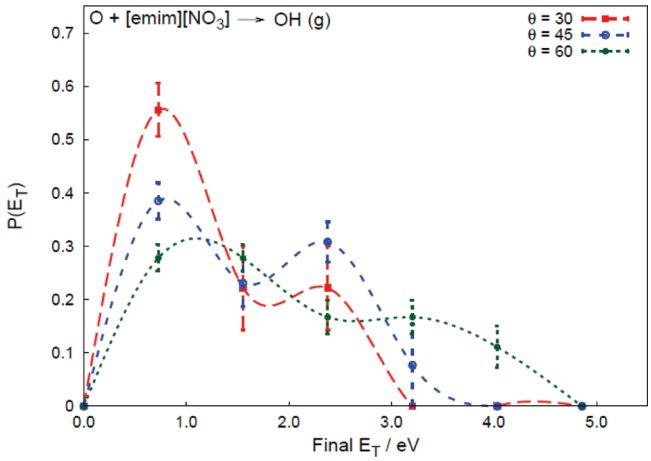

Figure 7. Distribution of the final translational energy (in eV) of Ar for incident angles (θ = 30, 45, and 60°).

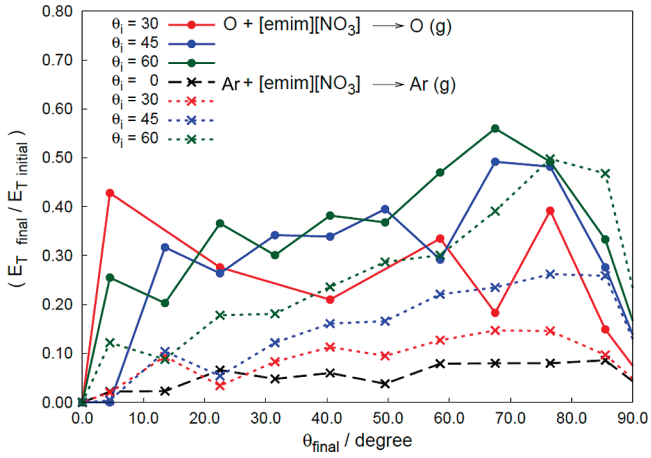

Figure 8. Distribution of the average ratio of the final to initial translational energy with respect to the final scattering angle for O and Ar.

of the incident atom, which is similar to what was found in the experimental collision studies of O + [emim][NTf_2].[39] In the O and OH scattering, there is a trend toward lower translational energy as the impact becomes more direct (smaller angles). However, this trend is not seen in Figures S2 and S3 of the Supporting Information for HNO_2 and HNO_3, respectively. The mechanism by which HNO_2 and HNO_3 leave the surface is more likely to be the result of a proton-transfer event rather than the collision impact. For HNO_2, there is a large portion of the nascent product that leaves the surface with ~0.5 eV of translational energy and a smaller group that leaves with ~2.0 eV. The nascent product HNO_3 has the narrowest distribution of final translational energy, which is centered on 1.0 eV. Furthermore, neither HNO_2 or HNO_3 leave with a translational energy larger than 2.5 eV, whereas the OH distribution has a significant amount of product with a final translational energy above 2.5 eV.

A further analysis of the interplay between final angle and translational energy of the desorption products is shown in Figures 8 and 9, grouped by incident angle. Figure 8 compares the scattered O and Ar distributions from [emim][NO_3], and we see that for the most part, the final translational energy increases as final angle increases up to a maximum at around 70−80°. This demonstrates that upon an increase in deflection (i.e., glancing collisions that result in larger θ_f), more of the initial translational energy is conserved in the final product. The incident Ar, on average, loses more of its initial translational

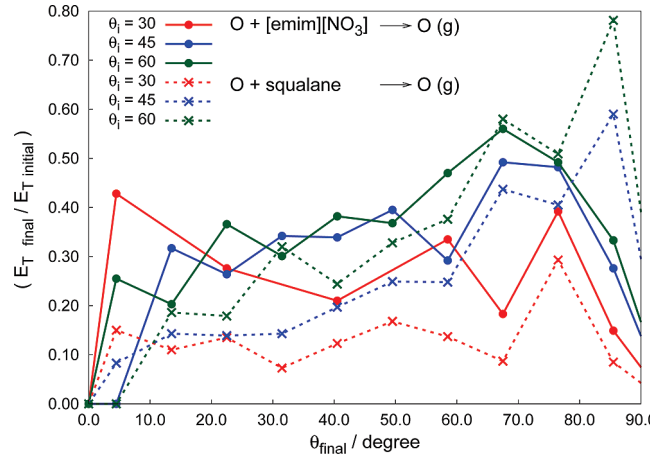

Figure 9. Distribution of the average ratio of the final to initial translational energy with respect to the final scattering angle for O scattering off of [emim][NO_3] and squalane. The squalane data is from ref 37.

energy to the surface in comparison to the scattered O. As a reminder, the values for the O with θ_i = 30° contain large error bars, as shown in Figure 5, and therefore, the somewhat erratic results for this data set are not significant.

In Figure 9, we compare the scattered O results for [emim][NO_3] with the previously studied squalane results.[37] Here, we see that squalane exhibits a trend similar to that seen for [emim][NO_3], where the larger θ_f leads to less energy transfer into the surface. Indeed, there is a remarkable similarity between the two liquids in how the translational energy changes with θ_f. However, the squalane surface can absorb more of the initial translational energy, which is remarkable given that the density of squalane is only half of that of [emim][NO_3]. In fact, Peng et al. have shown that upon impact with Ne, squalane will absorb most of the initial translational energy within the first few collisions.[51] Thus, squalane is the softer surface, allowing for deeper penetration of the O and therefore more energy transfer. Similar experimental data have been found in comparing the scattered products O and OH from the [emim][NTf_2], [C_{12}mim][NTf_2], and squalane surfaces.[39,52]

IV. Conclusions

In this paper, we have extended our QM/MM-MD model to simulate reactive and nonreactive collisions of O(^{3}P) and Ar with the RTIL surface [emim][NO_3]. This study provides some of the first qualitative characterization of the chemical reactivity of a RTIL surface. We compared the results to our previous theoretical model of O(^{3}P) + squalane and to a related experimental collision study by Minton et al. on O(^{3}P) + [emim][NTf_2] and [C_{12}mim][NTf_2]. Similar to other RTIL, [emim][NO_3] contains an increased density at the surface, with the largest nonpolar group (ethyl) sticking out of the surface; therefore, many of the collision results are determined by these properties.

The collision results provided herein should give a reasonable estimate of the actual system since they are based upon MSINDO energetics and quasi-classical trajectories. However, they are not at the level of advanced ab initio molecular dynamics. Upon collision with the [emim][NO_3] surface, more than 90% of the Ar are scattered from the surface. In addition, these collisions typically result in 2−3 proton transfers occurring between the imidazolium ring and the anion, and proton transfer enables a small fraction of the neutral emim and HNO_3 to desorb

from the surface within the 7.3 ps time limit of our simulation. Collisions with O lead to a vast array of bond-making and bond-breaking events with four main collision types, elimination of NO_3 forming species like [NO_2] and O_2, O addition to the imidazolium ring causing ring scission, H abstraction from hydrocarbon chains (ethyl or methyl) or an imidazolium ring generating OH, and O inelastic scattering. The O atom collisions also result in 1−2 proton transfers on average. The prominent gas-phase products from the O(^{3}P) reactions are all neutral and include OH, HNO_2, HNO_3, and emim. Additionally, our model predicts a small probability that a cluster of molecules desorb from the surface as a result of the O collisions and even less frequently as a result of the Ar collisions.

Both the scattered Ar and O have similar distributions of final translational energy, with the largest loss in incident energy at the most direct angles of incidence. The OH product from the reactive collisions results in a broad distribution in final translational energies, similar to that for the scattered O, with significant probability for energies above 2.0 eV. In contrast, for the HNO_2 and HNO_3 products, none of final translation energies are above ∼2.0 eV, and both products have a narrower distribution of final translation energies. These differences arise because HNO_2 and HNO_3 are primarily determined by proton transfer, which is not directly coupled to the incident oxygen, while the OH product is mostly from a direct H-abstraction mechanism. The proton-transfer mechanism also leads to similar scattering probabilities for emim and HNO_3 from both the Ar and O collisions. Although we do not have experimental data for the O + [emim][NO_3] system to compare with, many of our results connect closely to recent studies of the O + [emim][NTf_2] and [C_{12}mim][NTf_2] systems, enabling us to provide mechanistic understanding to these experiments.

Acknowledgment. The authors thank Dongwook Kim for supplying us with the O + squalane reaction data that was used in Figure 9. This research was supported by AFSOR Grant FA550-07-1-0095.

Supporting Information Available: Table S1 and S2 and Figures S1−S3 This material is available free of charge via the Internet at http://pubs.acs.org.

References and Notes

(1) Walden, P. *Bull. Acad. Imper. Sci. St. Pertersbourg* **1914**, *8*, 405.
(2) Rogers, R. D., Seddon, K. R., Volkov, S., Eds. *Green Industrial Applications of Ionic Liquids*; Springer: New York, 2003.
(3) Holbrey, J. D.; Seddon, K. R. *Clean Prod. Process.* **1999**, *1*, 223.
(4) Welton, T. *Chem. Rev.* **1999**, *99*, 2071.
(5) Tempel, D.; Henderson, P.; Brzozowski, J.; Pearlstein, R.; Garg, D. U.S. Patent 7563308, 2009.
(6) Kerlé, D.; Ludwig, R.; Geiger, A.; Paschek, D. *J. Phys. Chem. B* **2009**, *113*, 12727.
(7) *Material Matters*; Aldrich Chemical Co, Inc: Milwaukee, WI, 2007; Vol. 2, No. 2.
(8) Giridhar, P.; Venkatesan, K.; Srinivasan, T.; Rao, P. V. *Electrochim. Acta* **2007**, *52*, 3006.
(9) Swatloski, R. P.; Spear, S. K.; Holbrey, J. D.; Rogers, R. D. *J. Am. Chem. Soc.* **2002**, *124*, 4974.
(10) Wu, B.; Rogers, R.; Reddy, R. *Novel ionic liquid thermal storage for solar thermal electric power systems*. In Proceeding of solar forum; Washington, D.C., 2001.
(11) Chiu, Y.; Dressler, R. A. In *Ionic Liquids IV*; Brennecke, J. F., Rogers, Seddon, R. D., Kenneth, R., Eds.; ACS Symposium Series 975; American Chemical Society: Washington, DC, 2009; Chapter 10.
(12) Chambreau, S. D.; Schneider, S.; Rosander, M.; Hawkins, T.; Gallegos, C. J.; Pastewait, M. F.; Vaghjiani, G. L. *J. Phys. Chem. A* **2008**, *112*, 7816.
(13) Schneider, S.; Hawkins, T.; Rosander, M.; Vaghjiani, G.; Chambreau, S.; Drake, G. *Energy Fuels* **2008**, *22*, 2871.
(14) Gannon, T. J.; Law, G.; Watson, P. R.; Carmichael, A. J.; Seddon, K. R. *Langmuir* **1999**, *15*, 8429.
(15) Law, G.; Watson, P. R.; Carmichael, A. J.; Seddon, K. R. *Phys. Chem. Chem. Phys.* **2001**, *3*, 2879.
(16) Law, G.; Watson, P. R. *Chem. Phys. Lett.* **2001**, *345*, 1.
(17) Iimori, T.; Iwahashi, T.; Kanai, K.; Seki, K.; Sung, J.; Kim, D.; Hamaguchi, H.; Ouchi, Y. *J. Phys. Chem. B* **2007**, *111*, 4860.
(18) Rivera-Rubero, S.; Baldelli, S *J. Phys. Chem. B* **2006**, *110*, 4756.
(19) Santos, C. S.; Baldelli, S. *J. Phys. Chem. B* **2007**, *111*, 4715.
(20) Iwahashi, T.; Miyamae, T.; Kanai, K.; Seki, K.; Kim, D.; Ouchi, Y. *J. Phys. Chem. B* **2008**, *112*, 11936.
(21) Rivera-Rubero, S.; Baldelli, S. *J. Am. Chem. Soc.* **2004**, *126*, 11788.
(22) Yan, T.; Li, S.; Jiang, W.; Gao, X.; Xi, B.; Voth, G. A. *J. Phys. Chem. B* **2006**, *110*, 1800.
(23) Bhargava, B. L.; Balasubramanian, S. *J. Am. Chem. Soc.* **2006**, *128*, 10073.
(24) Lynden-Bell, R.; Del Popolo, M. *Phys. Chem. Chem. Phys.* **2006**, *8*, 949.
(25) Nathanson, G. M.; Davidovits, P.; Worsnop, D. R.; Kolb, C. E. *J. Phys. Chem.* **1996**, *100*, 13007.
(26) King, M. E.; Fiehrer, K. M.; Nathanson, G. M.; Minton, T. K. *J. Phys. Chem. A* **1997**, *101*, 6556.
(27) Harper, W. W.; Nizkorodov, S. A.; Nesbitt, D. J. *J. Chem. Phys.* **2000**, *113*, 3670.
(28) Chorny, I.; Benjamin, I.; Nathanson, G. M. *J. Phys. Chem. B* **2003**, *108*, 995.
(29) Nathanson, G. M. *Annu. Rev. Phys. Chem.* **2004**, *55*, 231.
(30) Zolot, A. M.; Dagdigian, P. J.; Nesbitt, D. J. *J. Chem. Phys.* **2008**, *129*, 194705.
(31) Zolot, A. M.; Dagdigian, P. J.; Nesbitt, D. J. *J. Chem. Phys.* **2008**, *129*, 194705.
(32) Kelso, H.; Kohler, S. P. K.; Henderson, D. A.; McKendrick, K. G. *J. Chem. Phys.* **2003**, *119*, 9985.
(33) Kohler, S. P. K.; Allan, M.; Kelso, H.; Henderson, D. A.; McKendrick, K. G. *J. Chem. Phys.* **2005**, *122*, 024712.
(34) Kohler, S. P. K.; Allan, M.; Costen, M. L.; McKendrick, K. G. *J. Phys. Chem. B* **2006**, *110*, 2771.
(35) Kohler, S. P. K.; Allan, M.; Reed, S. K.; Westacott, R. E.; McKendrick, K. G. *J. Phys. Chem. B* **2006**, *110*, 11717.
(36) Li, G; Bosio, S. B. M.; Hase, W. L. *J. Mol. Struct.* **2000**, *556*, 43.
(37) Kim, D.; Schatz, G. C. *J. Phys. Chem. A* **2007**, *111*, 5019.
(38) Radak, B. K.; Yockel, S.; Kim, D.; Schatz, G. C. *J. Phys. Chem. A* **2009**, *113*, 7218.
(39) Minton, T.; Wu, B.; Zhang, J.; Mckendrick, K.; Slattery, J.; Yockel, S.; Schatz, G. C. Unpublished results.
(40) Canongia Lopes, J. N.; Deschamps, J.; Padua, A. A. H. *J. Phys. Chem. B* **2004**, *108*, 11250.
(41) Canongia Lopes, J. N.; Deschamps, J.; Padua, A. A. H. *J. Phys. Chem. B* **2004**, *108*, 2038.
(42) Wilkes, J. S.; Zaworotko, M. J. *J. Chem. Soc., Chem. Commun* **1992**, 965.
(43) Ponder, W.; Richards, F. M. *J. Comput. Chem.* **1987**, *8*, 1016.
(44) Ahlswede, B.; Ju, K. *J. Comput. Chem.* **1999**, *20*, 563.
(45) Ahlswede, B.; Ju, K. *J. Comput. Chem.* **1999**, *20*, 572.
(46) Jug, K.; Chiodo, S.; Calaminici, P.; Avramopoulos, A.; Papadopoulos, M. G. *J. Phys. Chem. A* **2003**, *107*, 4172.
(47) Raabe, G.; Wang, Y.; Fleischhauer, J. *Z. Naturforsch.* **2000**, *55*, 687.
(48) Balasubramanian, R.; Wang, W.; Murray, R. W. *J. Am. Chem. Soc.* **2006**, *128*, 9994.
(49) Lynden-Bell, R. M. *Mol. Phys.* **2003**, *101*, 2625.
(50) Yan, T.; Li, S.; Jiang, W.; Gao, X.; Xiang, B.; Voth, G. A. *J. Phys. Chem. B* **2006**, *110*, 1800.
(51) Peng, Y.; Li, L.; Cao, Z.; Li, S.; Mazyar, O. A.; Hase, W. L.; Yan, T. *J. Phys. Chem. C* **2008**, *112*, 20340.
(52) Waring, C.; Bagot, P. A. J.; Slattery, J. M.; Costen, M. L.; McKendrick, K. C. *J. Phys. Chem. Lett.* **2010**, *1*, 429.

JP910707V